

High-Specificity In Vivo Tumor Imaging Using Bioorthogonal NIR-IIb Nanoparticles

Zichao Luo, Dehong Hu, Duyang Gao, Zhigao Yi, Hairong Zheng, Zonghai Sheng,* and Xiaogang Liu*

Lanthanide-based NIR-IIb nanoprobe are ideal for in vivo imaging. However, existing NIR-IIb nanoprobe often suffer from low tumor-targeting specificity, limiting their widespread use. Here the application of bioorthogonal nanoprobe with high tumor-targeting specificity for in vivo NIR-IIb luminescence imaging and magnetic resonance imaging (MRI) is reported. These dual-modality nanoprobe can enhance NIR-IIb emission by 20-fold and MRI signal by twofold, compared with non-bioorthogonal nanoprobe in murine subcutaneous tumors. Moreover, these bioorthogonal probe enable orthotopic brain tumor imaging. Implementation of bio-orthogonal chemistry significantly reduces the nanoprobe dose and hence cytotoxicity, providing a paradigm for real-time in vivo visualization of tumors.

1. Introduction

Near-infrared light in the second optical window (e.g., NIR-IIb, 1500–1700 nm) is ideal for visualizing living organisms with high spatiotemporal resolution because of its deep-tissue penetration capability, low photon scattering, and negligible autofluorescence.^[1] Existing NIR-IIb imaging probes, including carbon nanotubes,^[2] organic dyes,^[3] semiconducting polymers,^[4] inorganic nanoparticles,^[5] and quantum dots,^[1c] are constrained by low biocompatibility, inadequate chemical stability and photostability, and broad emission bands.^[6] In this regard, lanthanide-doped biocompatible nanoparticles with high chemical stability, enhanced photostability, and sharp

emission bandwidths^[7] have been explored as promising NIR-IIb nanoprobe for in vivo tumor imaging,^[8] dynamic monitoring of cancer immunotherapy,^[9] and tumor subtype identification.^[10] Despite these attributes, lanthanide-based imaging nanoprobe often display limited target specificity, thereby resulting in weak luminescent signals for in vivo tumor detection.^[11]

To overcome such limitations, the nanomedicine community has developed functional nanoprobe that are modified with active targeting ligands, including folic acid, nucleic acids, monoclonal antibodies, or peptides.^[12] These ligands

can target natural receptors expressed by tumor cells, which improves nanoprobe accumulation at tumor sites. Despite progress made, these strategies have significant limitations associated with limited bioreceptor expression on tumor cells, low receptor-to-ligand binding efficiency, and undesired receptor overexpression on healthy tissues.^[13]


Here we introduce a robust bioorthogonal approach to improving the targeting specificity of lanthanide-based NIR-IIb nanoprobe, enabling dual-model in vivo tumor visualization (Figure 1a). In our design, a metabolic substrate with a bioorthogonal azide group is first modified as a chemical receptor on tumor cell surfaces through metabolic engineering.^[14] A nanoprobe comprising the complementary alkyne group is then introduced to label the metabolic substrate. This strategy offers more effective tumor targeting than conventional strategies because of high-efficiency covalent ligation and abundant artificial receptors. Compared to non-bioorthogonal counterparts in tumor-bearing mouse models, our bioorthogonal nanoprobe can result in a 20-fold increase in NIR-IIb luminescence signals or enable target imaging with a fivefold reduction in the nanoprobe dose.

2. Results and Discussion

As a proof of concept, we designed and synthesized multilayer nanoparticles with a set of dopant ions incorporated into the core and shell layers (Figure 1b). We first synthesized NaYF₄ core nanoparticles tridoped with Yb³⁺, Er³⁺, and Ce³⁺ using a coprecipitation method. Subsequently, a thin shell doped with Nd³⁺ ions was epitaxially grown onto the core nanoparticles. To suppress surface quenching, we further introduced a NaGdF₄

Z. Luo, Z. Yi, X. Liu
Department of Chemistry and The N.I Institute for Health
National University of Singapore
Singapore 117543, Singapore
E-mail: chmlx@nus.edu.sg

D. Hu, D. Gao, H. Zheng, Z. Sheng
Paul C. Lauterbur Research Center for Biomedical Imaging
Key Laboratory for Magnetic Resonance and Multimodality Imaging of
Guangdong Province
Shenzhen Key Laboratory of Ultrasound Imaging and Therapy
CAS key laboratory of health informatics
Institute of Biomedical and Health Engineering
Shenzhen Institute of Advanced Technology
Chinese Academy of Sciences
Shenzhen 518055, P. R. China
E-mail: zh.sheng@siat.ac.cn

 The ORCID identification number(s) for the author(s) of this article can be found under <https://doi.org/10.1002/adma.202102950>.

DOI: 10.1002/adma.202102950

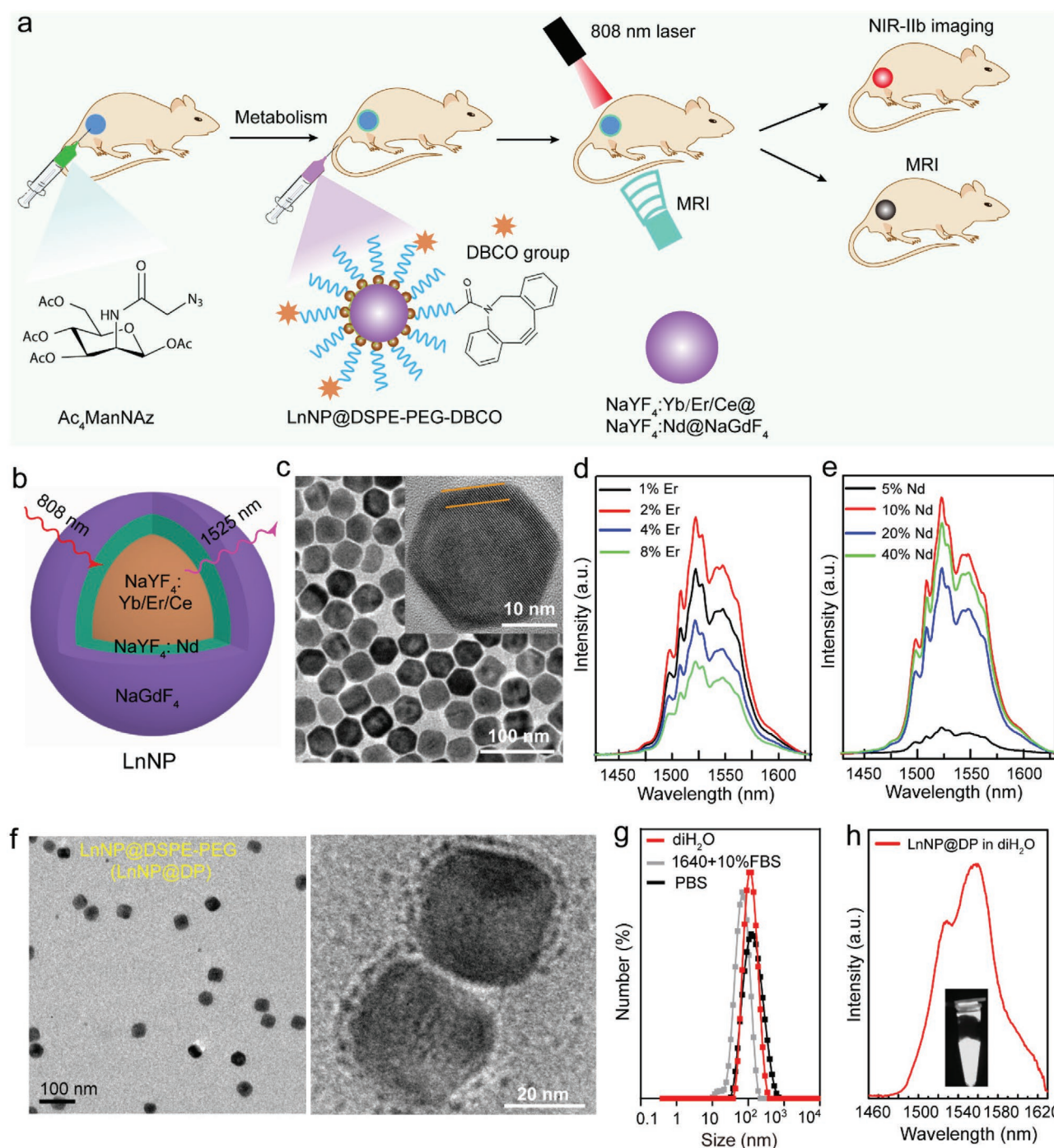


Figure 1. Characterization of NaGdF₄:Yb/Er/Ce@NaYF₄:Nd@NaGdF₄ nanoparticles. a) Biofunctionalization of multilayer nanoparticles (LnNP@DSPE-PEG-DBCO) for dual-modal tumor imaging. b) Schematic of the nanoprobe design. c) TEM image of the as-synthesized multilayer nanoparticles. Insert is a high-resolution TEM image of the multilayer nanoparticle. Orange lines denote the second shell (NaGdF₄). d) and e) Photoluminescence spectra of multilayer nanoparticles with different d) Er³⁺ or e) Nd³⁺ concentrations (excitation, 808 nm). f) TEM images of polymer-modified nanoparticles (LnNP@DSPE-PEG). g) Dynamic light scattering analysis of polymer-modified nanoparticles dispersed in water, phosphate-buffered saline (PBS) or Roswell Park Memorial Institute (RPMI) 1640 medium with 10% fetal bovine serum (FBS). h) Photoluminescent spectrum of nanoparticles measured under 808-nm irradiation. Inset is the corresponding photograph of NIR IIb-emitting nanoparticles under 808-nm excitation.

layer to core-shell nanoparticles (Figure S1, Supporting Information). As an added benefit, paramagnetic Gd³⁺ ions in the NaGdF₄ shell make these nanoparticles ideal for magnetic resonance imaging (MRI).^[15] Transmission electron microscopy

(TEM) imaging showed that these multilayer nanoparticles have an average size of ~ 38 nm (Figure 1c). High-resolution TEM imaging revealed a clear shell coating on the surfaces of core nanoparticles (Figure 1c). In addition, high-resolution

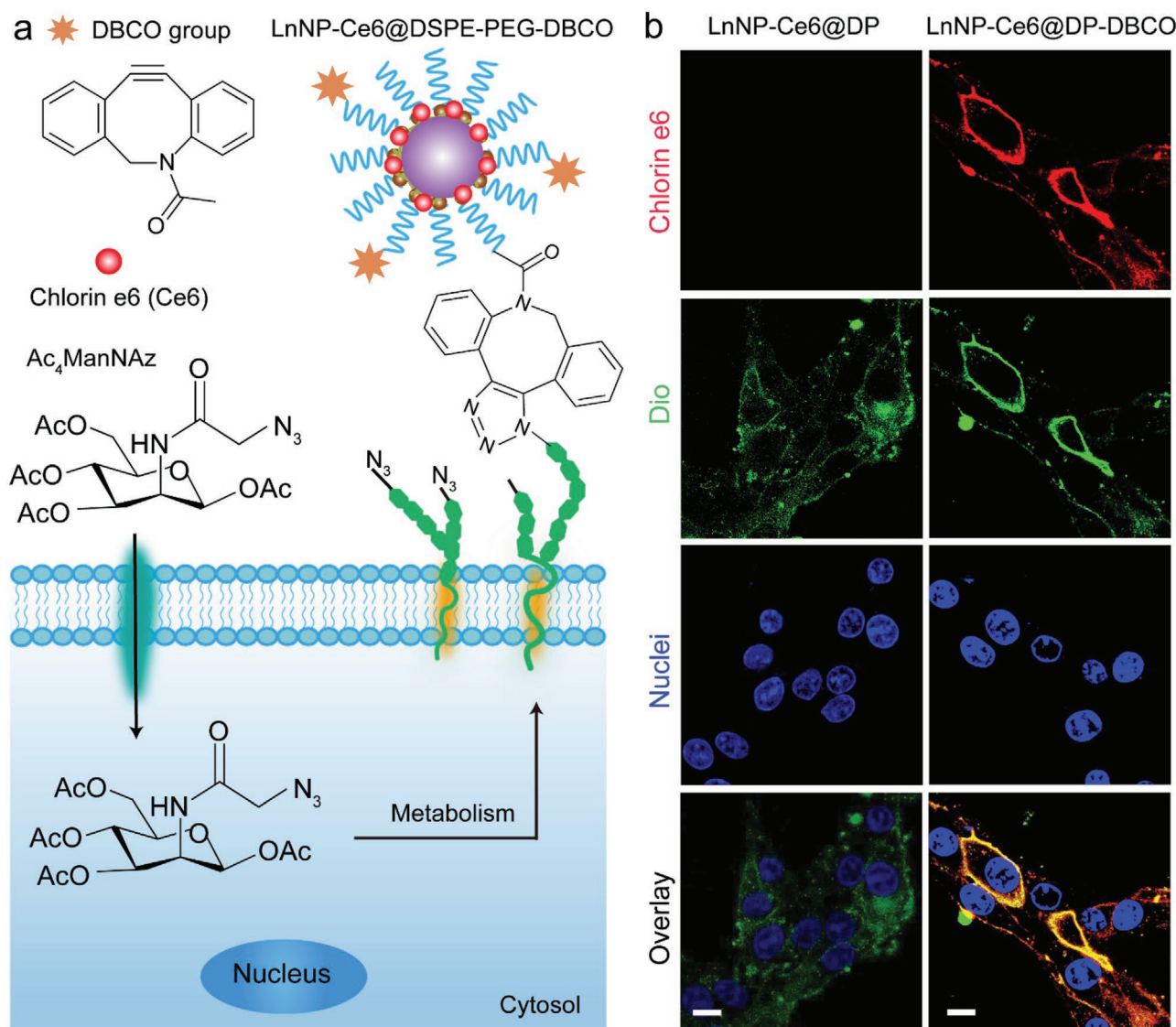


Figure 2. Copper-free click reaction-based in vitro luminescence imaging. a) Schematic of cell labeling using polymer-coated nanoparticles (LnNP-Ce6@DSPE-PEG-DBCO). An azide-labeled sugar (*N*-azidoacetylmannosamine-tetraacylated, Ac₄ManNAz) was first incubated with C6 cells to produce unnatural sialic acids with azide groups on cell membranes through metabolic engineering. Then, nanoparticles modified with an amphiphilic polymer comprising dibenzyl cyclooctyne (DBCO), a bioorthogonal group reactive to the azide group through copper-free click reaction, were added. b) Confocal images of C6 cells treated with Ac₄ManNAz (50 μM) and chlorin e6-labeled nanoparticles (20 min). Red: chlorin e6 for nanoprobe labeling; Green: Dio for cell membrane labeling. Blue: Hoechst for cell nucleus labeling. Scale bar: 10 μm.

TEM imaging and X-ray powder diffraction analysis of nanoparticles revealed their single-crystalline hexagonal phase (Figure S2, Supporting Information). Nd³⁺ in the middle shell was designed as the sensitizer for 808-nm light harvesting. Subsequently, excitation energy can be transferred from the Nd³⁺ shell to the Yb³⁺ core and then delivered to Er³⁺ for NIR-II emission (Figure S3, Supporting Information). Notably, Ce³⁺ was co-doped with Yb³⁺/Er³⁺ in the core to suppress upconversion, thus boosting down-shifting luminescence.^[1a] Separate doping of Yb³⁺/Er³⁺ and Nd³⁺ in different layers minimizes deleterious cross-relaxation of the excitation energy.

We next studied the optical properties of NaGdF₄:Yb/Er/Ce@NaYF₄:Nd@NaGdF₄ nanoparticles. Under irradiation with a continuous-wave 808-nm laser, nanoparticles showed

intense emission at approximately 1525 nm, corresponding to the ⁴I_{13/2}→⁴I_{15/2} transition (Figure 1d; and Figure S3, Supporting Information). We further optimized the doping concentrations of Er³⁺ and Nd³⁺ in multilayer nanoparticles. Optimal concentrations of Er³⁺ and Nd³⁺ are 2% and 10%, respectively (Figure 1d,e; and Figure S4, Supporting Information). To improve nanoparticle dispersibility under physiological conditions, we coated nanoparticles with a polyethylene glycol-based amphiphilic polymer (Figure S5, Supporting Information). TEM imaging showed that nanoparticles were coated with a 4-nm amorphous layer (Figure 1f), suggesting successful polymer encapsulation. Dynamic light scattering analysis showed that the particle size in water is approximately 90 nm (Figure 1g). When dispersed in phosphate-buffered saline or

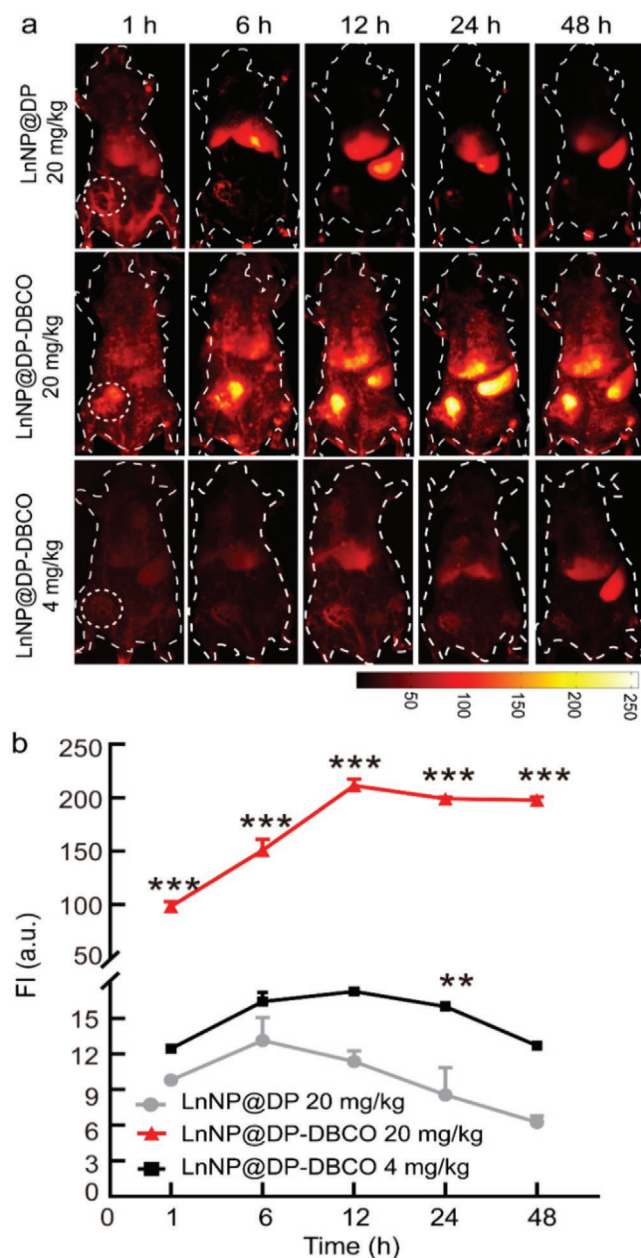


Figure 3. NIR-II fluorescence images for enhanced in vivo tumor detection in subcutaneous C6 tumors. C6 tumor-bearing mice were intratumorally injected with Ac₄ManANz (50 μ M) once a day for 3 days. After 24 h, DBCO-functionalized nanoparticles and controls were intravenously injected into the mice. a) Fluorescence imaging of C6 tumors at different intervals using lanthanide-doped nanoparticles (808 nm laser, 150 mW/cm²). b) Fluorescence intensities at the C6 tumor site corresponding to different time intervals. Dotted circles indicate tumor sites. All statistical data are shown as means \pm s.e.m. ($n = 3$ biologically independent samples; asterisk: LnNP@DP nanoparticles versus other treatments, **: $p < 0.05$, ***: $p < 0.001$. One-way ANOVA analysis with Tukey test).

cell culture medium (Roswell Park Memorial Institute (RPMI) 1640 medium with 10% fetal bovine serum), these nanoparticles retained a narrow size distribution (approximately 90 nm), and no obvious aggregation was observed (Figure 1g and Figure S6, Supporting Information). Under 808-nm excitation,

intense NIR-IIb luminescence was detected from nanoparticles dispersed in an aqueous solution (Figure 1h).

Prior to bioimaging, we evaluated the potential toxicity of amphiphilic polymer-modified NaGdF₄:Yb/Er/Ce@NaYF₄:Nd@NaGdF₄ nanoparticles in human umbilical vein endothelial cell (HUVEC) and bEnd.3 cell lines. All cell viabilities were over 85%, even at a particle concentration of 200 μ g/mL. Hemolytic analysis showed low hemolysis of only about 0.4% of red blood cells at a 400- μ g/mL particle concentration (Figure S7, Supporting Information). Taken together, these data suggest that the amphiphilic polymer-coated surface has good durability and biocompatibility.

Next, we performed NIR-II imaging of vessels of the whole mouse after intravenous injection of amphiphilic polymer-modified NaGdF₄:Yb/Er/Ce@NaYF₄:Nd@NaGdF₄ nanoparticles and used longpass filters (LP1000, LP1100, LP1320) to allow selected longer wavelengths to pass. Compared with imaging at 1000 and 1100 nm, NIR-II imaging with an LP1320 filter provides higher resolution and more accurate information in deep tissues due to reduced photon scattering and the low autofluorescence of normal tissues (Figure S8, Supporting Information). We next performed in vivo imaging of blood vessels and lymph nodes after different exposure times. Under 808-nm excitation, blood vessels, popliteal and sacral lymph nodes can be visualized (Figure S9, Supporting Information). However, for in vivo tumor imaging, we only detected weak luminescence at tumor sites, mainly because of the lack of target receptors on nanoparticle surfaces (Figure S10, Supporting Information).

To improve the nanoprobe's tumor-targeting ability, we introduced copper-free click chemistry that has been widely employed for rapid and selective labeling of biomolecules in living systems.^[16] In our study, an azide-labeled sugar (*N*-azidoacetylmannosamine-tetraacylated, Ac₄ManNAz) was first incubated with C6 glioma cells to produce artificial receptors such as azides on cell membranes through metabolic glycoengineering. Next, nanoprobes with polyethylene glycol-based polymer containing dibenzyl cyclooctyne (DBCO) groups were introduced to specifically react with artificial receptors on C6 glioma cell surfaces through a copper-free click reaction (Figure 2a). Notably, we encapsulated chlorin e6, a small, hydrophobic, NIR-emitting organic molecule, onto nanoprobe surfaces for confocal fluorescence microscopy. Upon incubation of DBCO-functionalized nanoprobes with Ac₄ManNAz-treated C6 cells, intense fluorescence of chlorin e6 was visible from these cells (Figure 2b). With increased incubation time or nanoprobe concentration, we observed a gradual increase in fluorescence intensity (Figures S11 and S12, Supporting Information). In stark contrast, we did not detect any fluorescence signals from cells treated with non-DBCO-functionalized nanoparticles.

We next performed in vivo tumor-targeting imaging using bioorthogonal NIR-IIb nanoprobes. In a typical experiment, murine subcutaneous C6 tumors were chosen for studying the behavior of DBCO-functionalized nanoprobes in animal models. To obtain azide group-expressed tumors, Ac₄ManNAz was intratumorally injected for 3 days. The Western blot analysis showed that Ac₄ManNAz-treated tumor tissues exhibit much stronger band intensities than PBS-treated counterparts, indicating successful azide modification of Ac₄ManNAz-pretreated

tumor tissues (Figure S13, Supporting Information). Subsequently, NIR-IIb nanoprobes were intravenously injected. We observed intense luminescence at 1525 nm from the tumor 1 h after nanoprobe injection, indicating rapid accumulation of nanoprobes at the tumor site (Figure 3a). The fluorescence signal increased over time and reached a maximum after 12 h. In contrast, only weak NIR-IIb emission was detected from the tumor 6 h after intravenous injection of non-DBCO-functionalized nanoprobes. After 12 h, the NIR-IIb emission essentially disappeared. Luminescence intensity at the tumor site treated with DBCO-functionalized nanoprobes was approximately 20-fold higher than that of the control group (Figure 3b). More importantly, NIR-IIb emission from DBCO-functionalized nanoprobes retained after more than 48 h, particularly attractive for real-time in vivo tumor imaging. Moreover, even after a fivefold reduction in the nanoprobe dose, we could still detect NIR-IIb emission at the tumor site 24 h after nanoprobe injection (Figure 3a; and Figure S14, Supporting Information).

The blood-brain barrier is a protective layer that surrounds and protects brain tumors from foreign species, such as drug molecules or probes, thereby resulting in low efficacy delivery of drug molecules or probes to a brain tumor.^[17] To test the feasibility of bioorthogonal labeling for brain tumor imaging, we intravenously injected as-prepared nanoprobes into a mouse bearing an orthotopic C6 brain tumor. With DBCO-functionalized nanoprobes, we observed an 8-fold increase in the NIR-IIb signal from the brain tumor, compared with using non-functionalized control nanoprobes (Figure S15, Supporting

Information). These data suggest that bioorthogonal labeling enables highly efficient nanoprobe accumulation in brain tumors.

Considering paramagnetic properties of Gd^{3+} , Gd^{3+} -based nanoprobes could be an effective contrast agent for T_1 -MRI.^[18] We first monitored their longitudinal relaxivity changes as a function of Gd^{3+} concentration. T_1 -weighted phantom images showed an apparent increase in contrast signal with increasing nanoprobe concentration (Figure S16, Supporting Information). Longitudinal relaxivity (r_1) of the nanoprobes was $756 \text{ mM}^{-1} \text{ s}^{-1}$. To test bioorthogonal nanoprobes for targeted MRI imaging, we incubated DBCO-modified nanoprobes with $Ac_4\text{ManNAz}$ -treated C6 cells and monitored their in vitro longitudinal relaxivity. These cells showed intense contrast signal in MRI imaging, which was much brighter than that treated with cell culture medium or control nanoprobes without the DBCO group (Figure S16, Supporting Information).

We next used bioorthogonal nanoprobes for tumor-specific MRI imaging. In our study, DBCO-functionalized nanoprobes were intravenously injected into C6 tumor-bearing mice. T_1 -weighted MR images revealed that the tumor site was lightened 6 h after injection. In addition, 12 h after injection, MRI intensity at tumor sites of nanoprobe-treated mice was approximately 2-fold higher than that of the control without DBCO treatment. Importantly, the MRI signal at tumor sites was still intense even after 48 h. In contrast, when control nanoprobes were intravenously injected, the tumor was only lightened 12 h after injection and disappeared after 24 h (Figure 4a,c). This

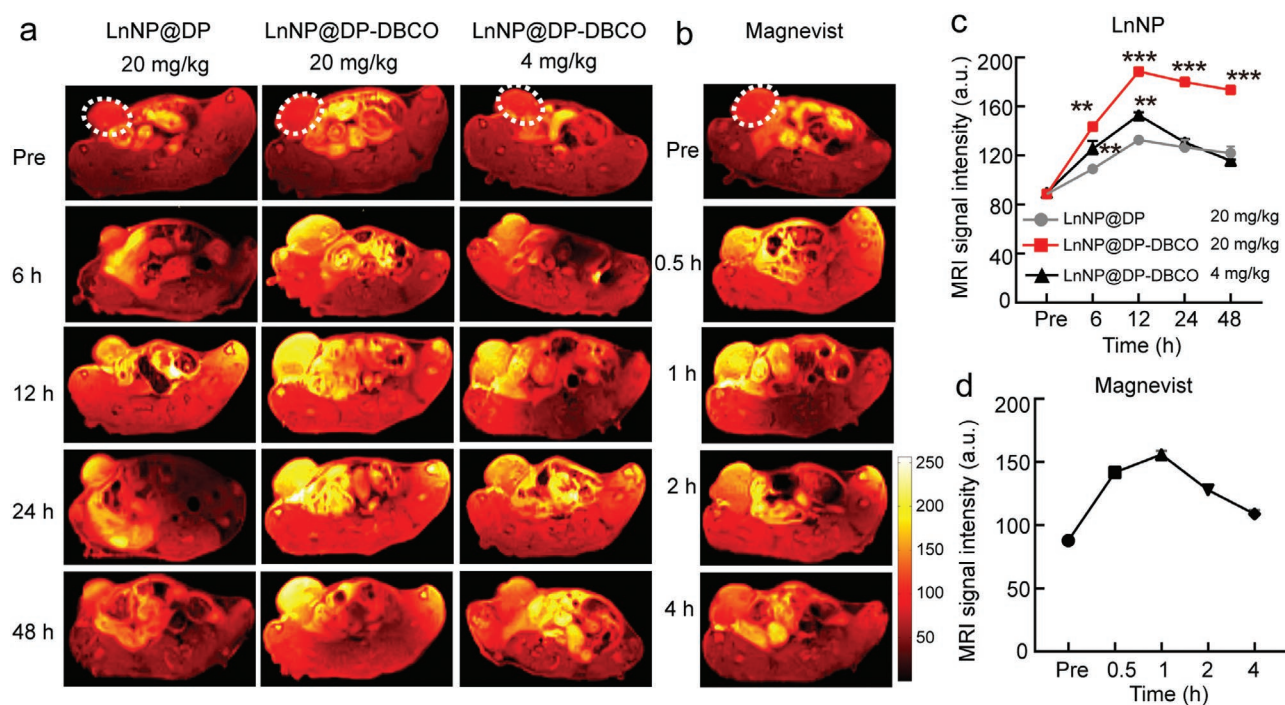


Figure 4. MRI images for enhanced in vivo tumor detection in subcutaneous C6 tumors. C6 tumor-bearing mice were intratumorally injected with $Ac_4\text{ManANz}$ (50 μM) once a day for 3 days. After 24 h, nanoprobes were intravenously injected into the above mice. a,b) Pseudocolor images of tumor-bearing mice after intravenous injection of: a) LnNP@DP (20 mg/kg, $2.5 \mu\text{mol Gd}^{3+}$) or LnNP@DP-DBCO nanoprobes (20 mg/kg, $2.5 \mu\text{mol Gd}^{3+}$ or 4 mg/kg, $0.5 \mu\text{mol Gd}^{3+}$) or b) Magnevist ($2.5 \mu\text{mol Gd}^{3+}$). c,d) MRI signal intensities at C6 tumor sites corresponding to different time points. Dotted circles indicate tumor sites. Data are shown as means \pm s.e.m. ($n = 3$ biologically independent samples; asterisk: LnNP@DP nanoprobes versus other treatments, **: $p < 0.05$, ***: $p < 0.001$. One-way ANOVA analysis with Tukey test).

result suggests that biorthogonal reactions can promote rapid nanoprobe accumulation at tumor sites. Notably, when the dose of DBCO-functionalized nanoprobe was reduced by 5-fold, the performance of T_1 -weighted MRI imaging of tumors was still better than the control nanoprobe, as determined by fast signal detection and enhanced MRI signal intensities at different time intervals. We further benchmarked nanoprobe targeting performance with Magnevist, a clinical MRI contrast agent.^[19] Tumor sites were lightened 0.5 h postinjection (Figure 4b,d). However, the MRI signal gradually weakened after 2 h and completely disappeared after 4 h. This short retention time in the tumor region is mainly attributed to the limited target specificity of Magnevist, which limits its clinical use for long-term MRI scanning.^[20]

DBCO-functionalized probes can also be used as target-specific contrast agents for orthotopic MRI of C6 brain tumors (Figure S17, Supporting Information). We further assessed in vivo cytotoxicity of the nanoprobe by performing hematoxylin and eosin (H&E) staining of major organs after intravenous injection for 7 days. H&E staining results revealed no obvious tissue injuries in the heart, liver, spleen, lungs, and kidneys (Figure S18, Supporting Information).

3. Conclusion

In conclusion, we have developed bioorthogonal lanthanide-based nanoprobe with high tumor-targeting specificity for deep-tissue NIR-IIb imaging and MRI. This targeting specificity greatly improves nanoprobe accumulation and retention at targeted tumor sites, which allows in vivo imaging to be achieved at a much smaller dose. We demonstrate that bioorthogonal nanoprobe offer an ≈ 20 -fold increase in the NIR-IIb imaging signal and a twofold increase in the MRI imaging signal, compared with non-orthogonal probes. In addition, strong NIR-IIb/MRI signals can be sustained for the whole observation period (>48 h), suggesting the utility of these nanoprobe for real-time, in vivo tumor visualization. Furthermore, bioorthogonal labeling facilitates nanoprobe accumulation in orthotopic brain tumors. These findings may provide a facile, robust strategy to support early detection of cancer.

Supporting Information

Supporting Information is available from the Wiley Online Library or from the author.

Acknowledgements

Z.L. and D.H. contributed equally to this work. This work was supported by the National Key & Program of China (Nos. 2018YFA0902600 and 2017YFE0120000), the National Natural Science Foundation of China (Nos. 21635002, 21771135, 21871071, 91859117, 81771906, and 81901812), the Ministry of Education, Singapore (No. MOE2017-T2-2-110), the Agency for Science, Technology and Research (A*STAR) (Grant Nos. A1883c0011 and A1983c0038), National Research Foundation, the Prime Minister's Office of Singapore under its NRF Investigatorship Programme (Award No. NRF-NRFI05-2019-0003), Science and Technology Key Project of Shenzhen (Nos. JCYJ20190812163614809 and JCYJ20200109114612308),

and Key Laboratory for Magnetic Resonance and Multimodality Imaging of Guangdong Province (No. 2020B1212060051).

Note: Figure 4 was replaced on December 7, 2021, after initial publication online, as the labels "4 mg/kg" and "20 mg/kg" columns 3 and 4 were marked in the wrong columns. Units for longitudinal relaxivity on page 5 were also corrected.

Conflict of Interest

The authors declare no conflict of interest.

Data Availability Statement

Research data are not shared.

Keywords

bio-orthogonal labeling, lanthanide-doped nanoparticles, MRI, NIR-IIb fluorescence, tumor imaging

Received: April 19, 2021

Revised: September 10, 2021

Published online: October 7, 2021

- [1] a) Y. Zhong, Z. Ma, S. Zhu, J. Yue, M. Zhang, A. L. Antaris, J. Yuan, R. Cui, H. Wan, Y. Zhou, *Nat. Commun.* **2017**, *8*, 737; b) S. He, J. Song, J. Qu, Z. Cheng, *Chem. Soc. Rev.* **2018**, *47*, 4258; c) M. Zhang, J. Yue, R. Cui, Z. Ma, H. Wan, F. Wang, S. Zhu, Y. Zhou, Y. Kuang, Y. Zhong, *Proc. Natl. Acad. Sci. USA* **2018**, *115*, 6590; d) S. Diao, J. L. Blackburn, G. Hong, A. L. Antaris, J. Chang, J. Z. Wu, B. Zhang, K. Cheng, C. J. Kuo, H. Dai, *Angew. Chem., Int. Ed.* **2015**, *54*, 14758.
- [2] Z. Ma, M. Zhang, J. Yue, C. Alcazar, Y. Zhong, T. C. Doyle, H. Dai, N. F. Huang, *Adv. Funct. Mater.* **2018**, *28*, 1803417.
- [3] a) S. Zhu, R. Tian, A. L. Antaris, X. Chen, H. Dai, *Adv. Mater.* **2019**, *31*, 1900321; b) Y. Li, Z. Cai, S. Liu, H. Zhang, S. T. Wong, J. W. Lam, R. T. Kwok, J. Qian, B. Z. Tang, *Nat. Commun.* **2020**, *11*, 1255; c) J.-B. Li, H.-W. Liu, T. Fu, R. Wang, X. B. Zhang, W. Tan, *Trends Chem.* **2019**, *1*, 224; d) T. B. Ren, Z. Y. Wang, Z. Xiang, P. Lu, H. H. Lai, L. Yuan, X. B. Zhang, W. Tan, *Angew. Chem., Int. Ed.* **2021**, *60*, 800.
- [4] a) Y. Jiang, P. K. Upputuri, C. Xie, Z. Zeng, A. Sharma, X. Zhen, J. Li, J. Huang, M. Pramanik, K. Pu, *Adv. Mater.* **2019**, *31*, 1808166; b) Y. Yang, S. Wang, L. Lu, Q. Zhang, P. Yu, Y. Fan, F. Zhang, *Angew. Chem., Int. Ed.* **2020**, *59*, 18380; c) Y. Yang, X. Fan, L. Li, Y. Yang, A. Nuernisha, D. Xue, C. He, J. Qian, Q. Hu, H. Chen, *ACS Nano* **2020**, *14*, 2509.
- [5] a) Q. Wang, Y. Zhan, S. Ling, H. Huang, Y. Zhang, G. Chen, S. Huang, C. Li, W. Guo, *Angew. Chem., Int. Ed.* **2021**, *60*, 2637; b) P. Zhu, S. Gao, H. Lin, X. Lu, B. Yang, L. Zhang, Y. Chen, J. Shi, *Nano Lett.* **2019**, *19*, 2128.
- [6] a) C. Li, Q. Wang, *ACS Nano* **2018**, *12*, 9654; b) Y. Zhong, H. Dai, *Nano Res.* **2020**, *13*, 1281; c) J.-n. Liu, W. Bu, J. Shi, *Chem. Rev.* **2017**, *117*, 6160; d) N. D. Barth, R. Subiros-Funosas, L. Mendive-Tapia, R. Duffin, M. A. Shields, J. A. Cartwright, S. T. Henriques, J. Sot, F. M. Goñi, R. Lavilla, *Nat. Commun.* **2020**, *11*, 4027.
- [7] a) N. M. Idris, M. K. Gnanasamandhan, J. Zhang, P. C. Ho, R. Mahendran, Y. Zhang, *Nat. Med.* **2012**, *18*, 1580; b) L. Zhou, R. Wang, C. Yao, X. Li, C. Wang, X. Zhang, C. Xu, A. Zeng, D. Zhao, F. Zhang, *Nat. Commun.* **2015**, *6*, 6938; c) Y. Dai, H. Xiao, J. Liu,

- Q. Yuan, P. a. Ma, D. Yang, C. Li, Z. Cheng, Z. Hou, P. Yang, *J. Am. Chem. Soc.* **2013**, 135, 18920; d) J. Wang, T. Wei, X. Li, B. Zhang, J. Wang, C. Huang, Q. Yuan, *Angew. Chem., Int. Ed.* **2014**, 53, 1616; e) M. Zhao, R. Wang, B. Li, Y. Fan, Y. Wu, X. Zhu, F. Zhang, *Angew. Chem., Int. Ed.* **2019**, 58, 2050; f) G. Xu, Q. Yan, X. Lv, Y. Zhu, K. Xin, B. Shi, R. Wang, J. Chen, W. Gao, P. Shi, *Angew. Chem., Int. Ed.* **2018**, 57, 3626; g) F. Wang, R. Deng, J. Wang, Q. Wang, Y. Han, H. Zhu, X. Chen, X. Liu, *Nat. Mater.* **2011**, 10, 968; h) G. Hong, A. L. Antaris, H. Dai, *Nat. Biomed. Eng.* **2017**, 1, 0010; i) H. Zhang, Y. Fan, P. Pei, C. Sun, L. Lu, F. Zhang, *Angew. Chem., Int. Ed.* **2019**, 58, 10153; j) M.-K. Tsang, G. Bai, J. Hao, *Chem. Soc. Rev.* **2015**, 44, 1585.
- [8] a) Y. Li, S. Zeng, J. Hao, *ACS Nano* **2019**, 13, 248; b) Z. Xue, S. Zeng, J. Hao, *Biomaterials* **2018**, 171, 153; c) P. Wang, Y. Fan, L. Lu, L. Liu, L. Fan, M. Zhao, Y. Xie, C. Xu, F. Zhang, *Nat. Commun.* **2018**, 9, 2898.
- [9] Y. Zhong, Z. Ma, F. Wang, X. Wang, Y. Yang, Y. Liu, X. Zhao, J. Li, H. Du, M. Zhang, *Nat. Biotechnol.* **2019**, 37, 1322.
- [10] Y. Fan, P. Wang, Y. Lu, R. Wang, L. Zhou, X. Zheng, X. Li, J. A. Piper, F. Zhang, *Nat. Nanotechnol.* **2018**, 13, 941.
- [11] J. He, C. Li, L. Ding, Y. Huang, X. Yin, J. Zhang, J. Zhang, C. Yao, M. Liang, R. P. Pirraco, *Adv. Mater.* **2019**, 31, 1902409.
- [12] a) S. Dharap, Y. Wang, P. Chandna, J. Khandare, B. Qiu, S. Gunaseelan, P. Sinko, S. Stein, A. Farmanfarmanian, T. Minko, *Proc. Natl. Acad. Sci USA* **2005**, 102, 12962; b) X. L. Hu, N. Kwon, K. C. Yan, A. C. Sedgwick, G. R. Chen, X. P. He, T. D. James, J. Yoon, *Adv. Funct. Mater.* **2020**, 30, 1907906.
- [13] a) Y. H. Bae, K. Park, *J. Controlled Release* **2011**, 153, 198; b) J. W. Park, K. Hong, D. B. Kirpotin, G. Colbern, R. Shalaby, J. Baselga, Y. Shao, U. B. Nielsen, J. D. Marks, D. Moore, *Clin. Cancer. Res.* **2002**, 8, 1172; c) T. A. Denison, Y. H. Bae, *J. Controlled Release* **2012**, 164, 187.
- [14] E. M. Sletten, C. R. Bertozzi, *Acc. Chem. Res.* **2011**, 44, 666.
- [15] H. Li, T. J. Meade, *J. Am. Chem. Soc.* **2019**, 141, 17025.
- [16] a) H. Y. Yoon, M. L. Shin, M. K. Shim, S. Lee, J. H. Na, H. Koo, H. Lee, J.-H. Kim, K. Y. Lee, K. Kim, *Mol. Pharmaceutics* **2017**, 14, 1558; b) J. B. Haun, N. K. Devaraj, S. A. Hilderbrand, H. Lee, R. Weissleder, *Nat. Nanotechnol.* **2010**, 5, 660; c) H. Koo, S. Lee, J. H. Na, S. H. Kim, S. K. Hahn, K. Choi, I. C. Kwon, S. Y. Jeong, K. Kim, *Angew. Chem., Int. Ed.* **2012**, 51, 11836; d) F. Hu, D. Mao, X. Cai, W. Wu, D. Kong, B. Liu, *Angew. Chem., Int. Ed.* **2018**, 57, 10182; e) W. Mao, J. Tang, L. Dai, X. He, J. Li, L. Cai, P. Liao, R. Jiang, J. Zhou, H. Wu, *Angew. Chem., Int. Ed.* **2021**, 60, 2393; f) M. R. Karver, R. Weissleder, S. A. Hilderbrand, *Angew. Chem., Int. Ed.* **2012**, 51, 920; g) D. Ye, A. J. Shuhendler, L. Cui, L. Tong, S. S. Tee, G. Tikhomirov, D. W. Felsner, J. Rao, *Nat. Chem.* **2014**, 6, 519.
- [17] a) C. D. Arvanitis, G. B. Ferraro, R. K. Jain, *Nat. Rev. Cancer* **2020**, 20, 26; b) Y. Zhou, Z. Peng, E. S. Seven, R. M. Leblanc, *J. Controlled Release* **2018**, 270, 290; c) A. G. de Boer, P. J. Gaillard, *Clin. Pharmacokinet.* **2007**, 46, 553.
- [18] a) J. S. Ananta, B. Godin, R. Sethi, L. Moriggi, X. Liu, R. E. Serda, R. Krishnamurthy, R. Muthupillai, R. D. Bolskar, L. Helm, *Nat. Nanotechnol.* **2010**, 5, 815; b) T. Courant, V. G. Roullin, C. Cadiou, M. Callewaert, M. C. Andry, C. Portefaix, C. Hoeffel, M. C. de Goltstein, M. Port, S. Laurent, *Angew. Chem., Int. Ed.* **2012**, 51, 9119; c) T. J. Clough, L. Jiang, K.-L. Wong, N. J. Long, *Nat. Commun.* **2019**, 10, 1420.
- [19] a) M. S. Nacif, A. E. Arai, J. A. Lima, D. A. Bluemke, *J. Cardiovasc. Magn. Reson.* **2012**, 14, 18; b) S. Anbu, S. H. Hoffmann, F. Carniato, L. Kenning, T. W. Price, T. J. Prior, M. Botta, A. F. Martins, G. J. Stasiuk, *Angew. Chem., Int. Ed.* **2021**, 60, 10736.
- [20] a) Z. Yi, Z. Luo, N. D. Barth, X. Meng, H. Liu, W. Bu, A. All, M. Vendrell, X. Liu, *Adv. Mater.* **2019**, 31, 1901851; b) J. ö. Barkhausen, W. Ebert, J. ö. F. Debatin, H.-J. Weinmann, *J. Am. Coll. Cardiol.* **2002**, 39, 1392.